Integration of broadband seismic data into reservoir characterization workflows: A case study from the Campos Basin, Brazil

Ekaterina Kneller[1] and Manuel Peiro[1]

Abstract

Towed-streamer marine broadband data have been key contributors to recent petroleum exploration history, in new frontiers and in mature basins around the world. They have improved the characterization of reservoirs by reducing the uncertainty in structural and stratigraphic interpretation and by providing more quantitative estimates of reservoir properties. Dedicated acquisition, processing, and quality control (QC) methods have been developed to capitalize on the broad bandwidth of the data and allow their rapid integration into reservoir models. Using a variable-depth steamer data set acquired in the Campos Basin, Brazil, we determine that particular care that should be taken when processing and inverting broadband data to realize their full potential for reservoir interpretation and uncertainty management in the reservoir model. In particular, we determine the QC implemented and interpretative processing approach used to monitor data improvements during processing and preconditioning for elastic inversion. In addition, we evaluate the importance of properly modeling the low frequencies during wavelet estimation. We find the benefits of carefully processed broadband data for structural interpretation and describe the application of acoustic and elastic inversions cascaded with Bayesian lithofacies classification, to provide clear interpretative products with which we were able to demonstrate a reduction in the uncertainty of the prediction and characterization of Santonian oil sandstones in the Campos Basin.

Introduction

The Campos Basin is located offshore Southeast Brazil and covers 115,000 km^2 along the northern coast of Rio de Janeiro state and the southern coast of Espirito Santo state. The Campos Basin is historically the most prolific Brazilian basin, accounting for 74% of Brazilian oil and 32% of national gas production in 2015 (Bastos, 2015). Exploration in the Campos Basin started in the late 1950s, and shallow-water oilfields were discovered in the 1970s. Deepwater fields, with turbidite reservoirs at various chronostratigraphic levels, were discovered in the 1980s and 1990s, and we are now in a phase of ultra-deepwater discoveries. The Xelerete concession, located 250 km off the coast of the Rio de Janeiro State, is one such discovery. The field, containing heavy oil, was discovered in 2001 in a water depth of 2400 m. Although a presalt prospect was later identified below the main clastic target, this paper focuses on the first postsalt discovery that was declared commercial in 2007 with, at the time, an estimated in-place volume of 1.4 billion boe (source: Petrobras press release, 09/10/2007).

Post-salt sandstones in the Campos Basin are characterized by complex depositional systems, showing high degrees of reworking and redistribution (Mutti and Carminatti, 2012) as shown in the schematic cross section in Figure 1. These systems are seismically highly anisotropic and heterogeneous, with sharply varying thicknesses and some volcanic intrusions. The geologic setting of the Campos Basin makes it challenging for seismic imaging, reservoir characterization, facies identification, and ultimately reservoir uncertainty management. Nevertheless, post- and presalt discoveries in the deepwater part of the basin have sustained the continuous demand for seismic exploration in the area.

In response to those challenges, CGG acquired a broadband multiclient seismic survey in the Campos Basin in 2014, covering an area of approximately 10,000 km^2. Being rich in low- and high-frequency contents, broadband data can image deeper targets, improve vertical resolution, and ultimately reduce the uncertainty in reservoir characterization. The benefits of such an acquisition configuration have been demonstrated in previous seismic imaging (Soubaras and Whiting, 2011; Masclet et al., 2015a) and seismic velocity model building work (Masclet et al., 2015b). The improvement in reservoir characterization conditioned by the wider frequency bandwidth of broadband seismic data has also been shown in previous case studies (Lafet et al., 2012; Reiser et al., 2012; Soubaras et al., 2012; Wallick and Giroldi, 2013; Kneller et al., 2013; and Michel and Sablon, 2016).

[1]CGG, GeoConsulting, Rio de Janeiro, Brazil. E-mail: ekaterina.kneller@cgg.com; manuel.peiro@cgg.com.

Manuscript received by the Editor 7 March 2017; revised manuscript received 12 August 2017; published ahead of production 08 November 2017; published online 21 December 2017. This paper appears in *Interpretation*, Vol. 6, No. 1 (February 2018); p. T145–T161, 30 FIGS.

http://dx.doi.org/10.1190/INT-2017-0049.1.

As for any type of seismic data, a fundamental principle remains true for broadband data: Reservoir characterization will only fully benefit from the seismic data if it is properly processed and imaged. This is achieved through new methods and algorithms that are better suited to the wider bandwidth, and, in particular, the low-frequency content of the data (Mesdag and Schakel, 2015; Soubaras, 2016) as well as the judicious choice of processing parameters coupled with quality control (QC) that makes it possible to assess signal preservation versus noise attenuation (Coleou et al., 2013). In this work, we propose to revisit some of the main steps in the seismic signal treatment and seismic inversion of broadband seismic data, using the Campos Basin variable-depth streamer seismic data set. The objective is to propose the best practices to help the interpreters to reduce the risk in oil exploration when broadband seismic data are used. The resulting study showcases the benefits that broadband data can bring to reservoir uncertainty management — in this case, at the exploration stage.

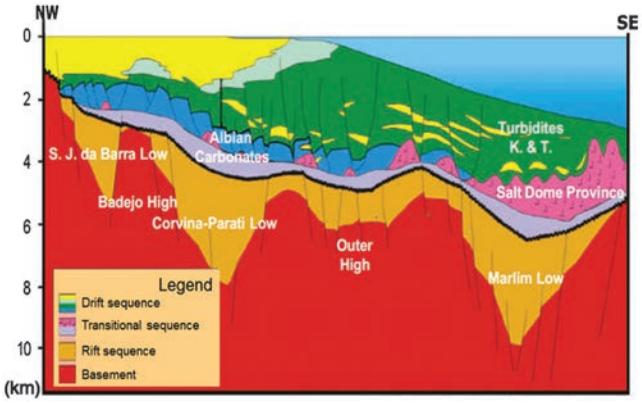

Figure 1. Schematic geological section of the Campos Basin (Marcos Andre Alves, Brazil Round 9, 2007). The interval of interest of this study is postsalt turbidities.

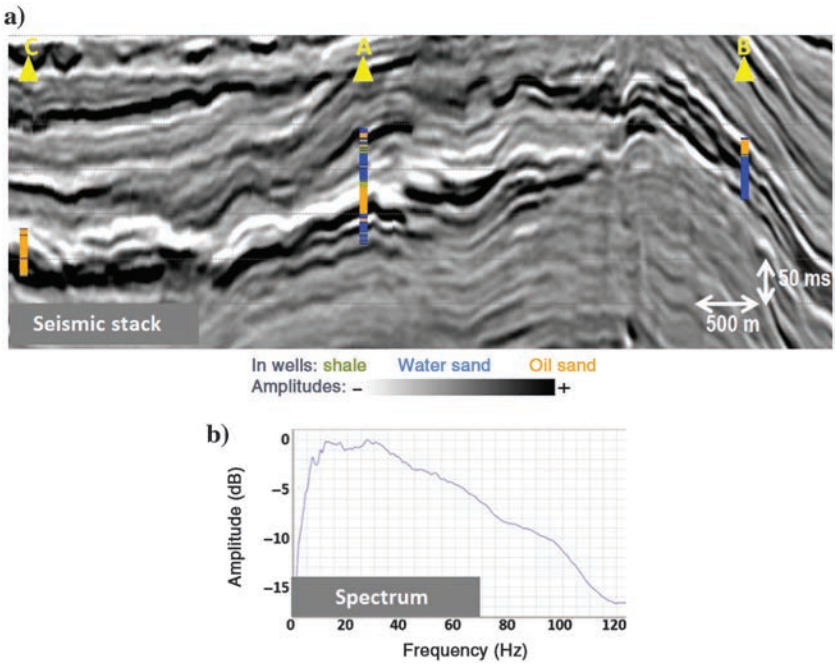

Figure 2. (a) Full-stack section through three wells C, A, and B and (b) amplitude spectrum calculated in a 1300 ms window centered on reservoir level.

Case study overview

Following the high interest in seismic exploration in the Campos Basin, a variable-depth streamer acquisition with 12 streamers, each 8100 m long, was acquired by CGG in 2014. The cable depth varied from 10 m at the near offset to 50 m at the farthest offset, and the source depth was 6 m.

The data processing sequence consisted of swell and linear noise removal, suppression of seismic interference, debubbling using the far-field source signature modeled from the recorded near-field hydrophone, ghost wavefield elimination (Hu et al., 2014), water column static correction to compensate for water temperature variations, 3D surface-related multiple attenuation, and regularization onto a 25×25 m grid. A prestack Kirchhoff depth-migration algorithm was used to perform the imaging after a geologically consistent velocity model had been built through a multilayer horizon-constrained tomography (Masclet et al., 2015b). At the target level, the amplitude spectrum of the final data calculated in a 1300 ms vertical window show the −6 dB bandwidth ranging from 4 to 68 Hz — see Figure 2.

An area of 100 km^2 encompassing three exploration wells drilled through postsalt clastic sediments of Santonian age was chosen for the present work.

A preliminary feasibility study based on rock-physics analysis was performed on the available well data in the area to determine if the elastic properties expected from seismic inversion would be able to effectively discriminate between the target lithology classes (based on a rock-physics petroelastic model). Three wells, A, B, and C, have compressional sonic and density logs available in the reservoir interval, and only well A has shear sonic log data. The target intervals of this study are the Santonian oil-bearing sandstones. The geophysical problem being solved here is the estimation of probability of their occurrence in the test area. Three types of lithofacies have been defined at the wells: shale, water sandstones, and oil sandstones. Figure 3 shows the acoustic impedance logs from the three wells, with the highlighted pay zones clearly showing lower impedance values. However, a statistical analysis of the lithofacies types (Figure 4) shows significant overlap among the rock types and impedance values

change significantly between wells. We propose explaining this overlap by the presence of a depth trend. Without removing this trend, we cannot apply cutoff impedance values to directly separate the oil-saturated sand from the other two zones. We therefore "detrend" the acoustic and elastic property values by subtracting the compaction trend, defined as a linear function of depth, from the log property values. This operation allows for more effective separation of the pay zone in the detrended acoustic impedance values (Figure 5) which, in turn, allows the acoustic inversion to separate the oil sands more effectively. Further analysis of the elastic properties in well A, where the S-wave velocity and other elastic properties are available, shows that the use of detrended lambda-rho and mu-rho elastic properties (Goodway, 2001) improves the separation of the pay zone interval from other facies (Figure 6).

The preceding well-log analysis showed that an elastic inversion of the seismic data for detrended lambda-rho and mu-rho will optimally characterize the oil-bearing sandstones and hence reduce the uncertainty of the pay zone localization. With the seismic field data as our main input, the broad outline of our reservoir characterization workflow is as follows:

- seismic data preconditioning
- horizon and fault interpretation
- spectral analysis and wavelet estimation
- optimization of the initial inversion model and parameters
- lithofacies definition and classification.

Each of the steps will be reviewed in detail in the next sections, focusing on the specific considerations for broadband data.

Seismic preconditioning and inversion workflow

Seismic data preconditioning

Although the main processing sequence is usually optimized to best address imaging-related issues, greater focus is placed on delivering final data that are ready to be input into quantitative analysis and reservoir characterization workflows — such as amplitude

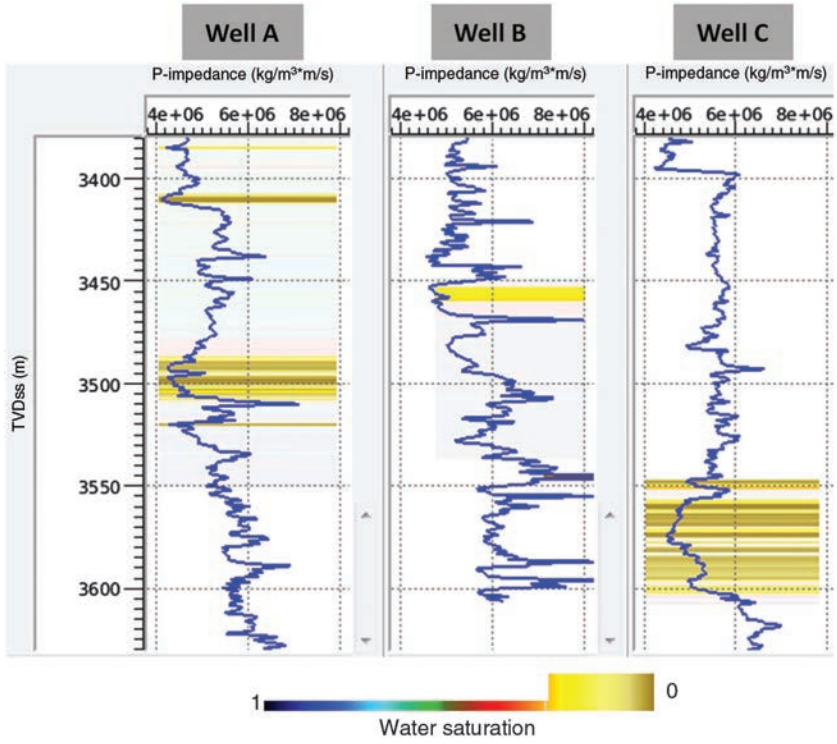

Figure 3. Acoustic impedance log in wells A, B, and C with pay zones highlighted by low values of water saturation.

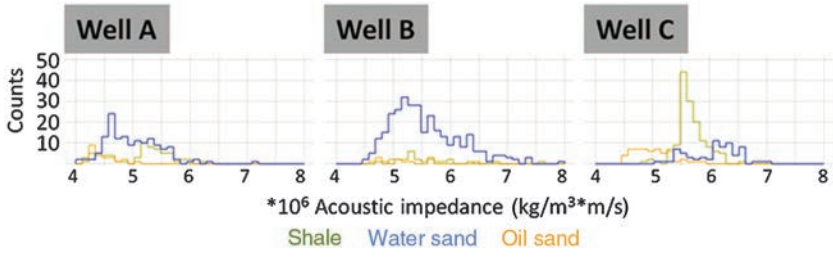

Figure 4. Histograms of acoustic impedance values color coded by rock type (shale, water-saturated sandstone, and oil-saturated sandstone) in wells A, B, and C. Impedance values for the same lithology change significantly between wells.

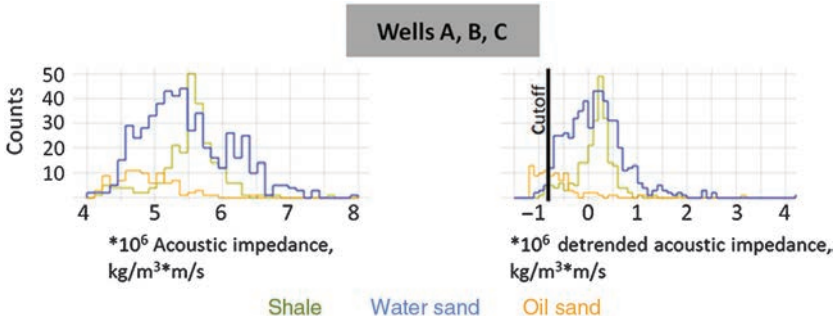

Figure 5. Rock-physics plot, wells A, B, and C — combined histogram of acoustic impedance values colored by rock type from three wells. Left: Before detrending, there is significant overlap of the rock types in terms of acoustic impedance values. Right: After detrending, it is possible to isolate some of the oil sand rock type using a detrended acoustic impedance cutoff ($-8.5e+06$ kg/m^3 $*$ m/s suggested here).

variation with offset (AVO) studies, direct hydrocarbon indicator (DHI) generation, or acoustic and elastic inversions. Depending on the final reservoir management objectives, additional enhancement steps can be undertaken to optimize the data. It is also worth stressing that, just as the processes applied are important, appropriate QCs should be put in place during data acquisition, processing, and preconditioning. Definition of the most relevant attributes, horizons over which they are analyzed, and statistics to be checked is preferably tailored as a function of the project's final objectives (Araman and Paternoster, 2014). By iterating the analysis of these attributes, it is possible to quantitatively monitor the improvement in the seismic data with respect to the final aim. Particular attention should be paid to the following points:

- wavelet stationarity — vertical and lateral variations in signal frequency, phase, and amplitudes
- levels of coherent and random noise and lateral consistency in the signal
- prestack signal variability in terms of frequency content, phase, and AVO
- calibration of the seismic data with other measured "hard" data such as well logs.

In the case of the present study, the geophysical problem being addressed is to best characterize the oil-bearing sandstone by inverting partial angle stacks for elastic properties. We therefore decided to combine two QC approaches:

- Local QC where well log data are available: Seismic rock-physics modeling help to assess if the data are locally calibrated and representative of the existing reservoir property knowledge. This ensures that rock properties can be retrieved from seismic amplitudes. We include the following in those steps: the well-to-seismic tie, AVO curve comparisons between seismic and synthetic, local deterministic wavelet analysis, and mini inversions in the well vicinity.
- Global QC via statistical parameters, calculated at the survey scale, to capture the global behavior of the signal: signal-to-noise ratio (S/N), quality and anomaly attributes for AVO QC (Coleou et al., 2013), and enhanced bandwidth at every preconditioning step. These QCs can be viewed globally or on selected horizons.

In short: tie the seismic to any other reliable data available, in our case log data, and use statistical QC indicators on a more global basis, including horizon-based QC, for stationarity analysis.

Three preconditioning procedures were performed on the data set, taking special care to preserve low-frequency content of the data:

- random noise attenuation applied to gathers
- structural filtering applied to angle stacks
- spectral shaping applied to angle stacks.

The projective filtering is carried out in the f-x domain. For this case study, stronger denoising parameters were chosen for the high frequencies compared with the low frequencies. This parameterization concentrates the energy of the residuals in the high-frequency range, which is more affected by random noise, and it better preserves the low frequencies. The filter parameters are optimized using residual analysis, AVO curve analysis before and after the filter application, and AVO attribute analysis to ensure that noise is attenuated without affecting the signal.

After gather preconditioning, the decision about angle intervals for partial stack calculation is taken through data evaluation, AVO analysis tests, and inversion tests. The angle intervals should include seismic data of sufficient quality and subsequently allow recovery of the elastic properties in prestack inversion. The angle stacks were defined as follows: 6°–18° (near), 16°–28° (mid), 26°–38° (far), and 36°–48° (ultra-far).

Structurally consistent filtering was applied to angle stacks: It filters along the local dips computed on the reference data. This filter decreases the energy of the low-frequency component of the data and depends significantly on the choice of reference data. This filter increases the S/N values in all angle stacks, and Figure 7 shows the result for the mid angle stack. There is a global increase in S/N extracted from the reservoir interval visible in the attribute maps (a shift from blue to red colors) and in the corresponding histograms of the S/N values for the reservoir interval.

After evaluation of the results, differences in the frequency spectrum of the partial stacks were observed (Figure 8), with the high-frequency part of the spectrum becoming weaker and the low-frequency part of the spectrum becoming more prominent as the offset increases. This is expected because attenuation of seismic energy is frequency dependent and increases with the travel path (i.e., the greater the offset, the greater the attenuation of the high frequencies).

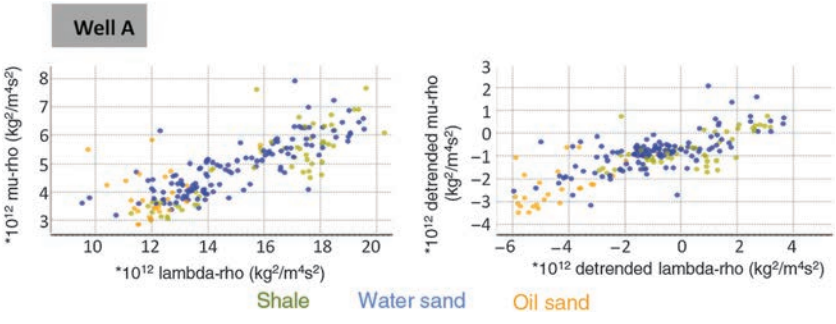

Figure 6. Rock-physics plot, well A — crossplot of lambda-rho versus mu-rho values. Top: before detrending; bottom: after the elastic properties have been detrended. The oil-saturated sand is better separated.

Spectral shaping was applied to angle gathers to improve the homogeneity of the frequency content between angle stacks. An individual matching operator was calculated for the mid, far, and ultra-far stacks, using the spectrum of the near stack as a reference. The calculation was done over a short time gate of 300 ms to avoid the influence of vertical nonstationarity in the frequency content of the data because no Q compensation in amplitude had been previously applied to the data. A representative set of traces was selected for the calculation because a single operator was derived for each partial stack and was applied globally. Figure 8 shows the spectra estimation for angle stacks before and after spectral shaping. A routine step in preconditioning workflows is a residual misalignment correction between angle stacks. This was tested on the full data set, but no indication of its benefits was found from a seismic inversion point of view (i.e., no obvious improvement in the well-to-seismic calibration, the global AVO behavior, or elastic inversion results was observed). An example gather is shown in Figure 9f.

Having elastic property logs available at well A, we were able to perform a local QC of the calibration of the seismic response to known measured data. We used the sonic, shear, and density logs to calculate the reflectivity at various incidence angles using the full Zoeppritz equations (1919). A synthetic prestack data set was then generated with a 1D convolutional model. These synthetic AVO gathers were compared with the real data at each step in the preconditioning sequence, making it possible to check the calibration of the AVO response of the seismic data to what is expected from measured log data. Figure 9 shows how the AVO response at the well A location was improved at each step in the preconditioning sequence (including spectral shaping) as shown by the decreasing dispersion of the points around the regression (which is preserved).

Coleou et al. (2013) introduce an efficient statistical tool that helps to quantify and monitor the AVO compliance of large amounts of prestack data, as well as identifying areas where further improvement in the data quality are required. Repeatability attributes called anomaly and quality, an orthogonalization of crosscorrelation and normalized rms amplitude (Nrms), are calculated between real traces and AVO model traces. Focusing the analysis of those attributes over the main interval of interest (approximately 400 ms centered on the Santonian interval) at various steps in the preconditioning sequence allowed us to statistically evaluate the improvement in the data. Maps of the quality attribute calculated for the reservoir interval at the beginning and end of the preconditioning sequence are displayed in Figure 10, illustrating how the similarity of the real and model traces increases during the preconditioning sequence for all the angle stacks across the extent of the study area. Figure 11 shows crossplots of the quality and anomaly attributes calculated in a 400 ms time window at the reservoir level at the beginning and end of the preconditioning sequence. After preconditioning,

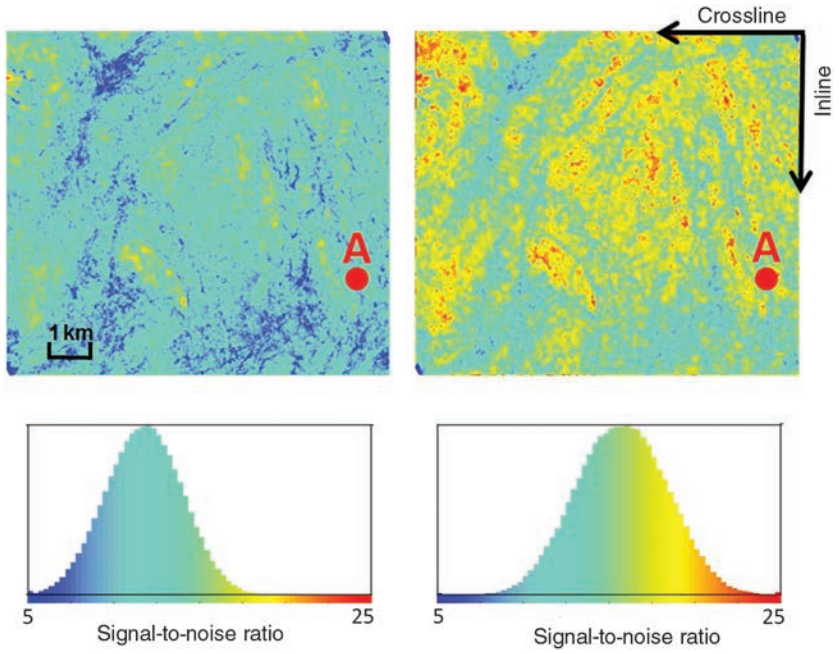

Figure 7. S/N (in dB) estimated in the reservoir interval before (left) and after (right) structurally consistent filter application for the midangle stack. Maps of the S/N are shown in the top panels along with the location of well A. The lower panels show the corresponding histograms of the S/N values and indicate the color scale for the maps.

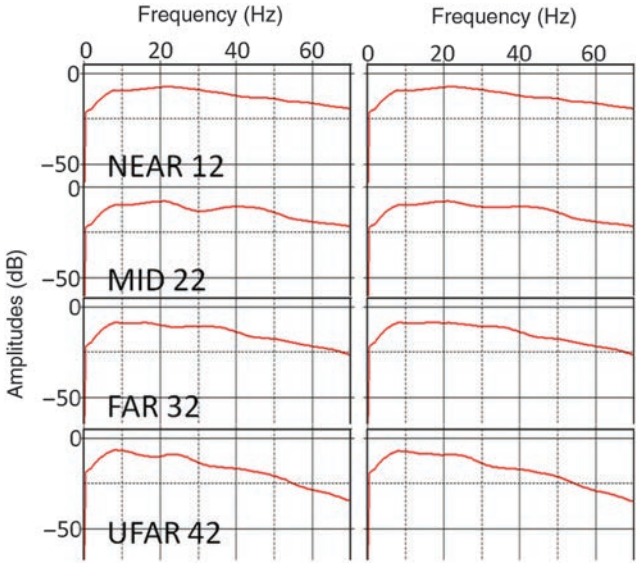

Figure 8. Amplitude spectra (in dB) for the angle stacks before (left) and after (right) spectral shaping.

there is a shift in the value to higher quality and lower anomaly, again indicating a quantitatively better fit between the real and model traces. Using these metrics, we were able to gauge the data quality as well as monitor the increase in confidence in the seismic data away from well A where we know it is calibrated during the preconditioning.

Interpretation of horizons and faults

The structural interpretation is usually performed before reservoir characterization and inversion, using the seismic amplitude data and seismic attribute analysis. It can be further refined after the seismic attributes and elastic properties have been calculated from the data. In the context of highly reworked geology, with faulting, potential large displacements, and lateral discontinuities in the seismic events, the low-frequency information contained in broadband data provides valuable information for the interpreter. Previous work, in particular by Duval (2012), has demonstrated the value of broadband data for structural interpretation. We further illustrate this with two examples, using our preconditioned full-stack seismic cube as input. We first performed manual picking of seismic events at the top and bottom of the interval of interest. Second, coherency-based attributes, routinely used for fault and fracture detection, were calculated. To evaluate the impact of low frequencies on those steps, they were performed on the full-bandwidth broadband data and after application of a 10 Hz low-cut filter.

During automatic picking, we observe that the seismic events on broadband data present a more unique waveform, due to the extended bandwidth and reduced side lobes. The resulting reduced uncertainty in picking can be seen in Figure 12, which shows the section views of full-bandwidth broadband seismic data (b) compared with the data without low frequencies (a), after the application of a 10 Hz low-cut filter. The bright negative reflection (black horizon) corresponds to the top, and the positive reflector corresponds to the bottom (red horizon) of the zone of interest. The character (waveform and amplitude) of these reflections is unique on broadband data and cannot be confused with other events, whereas this uniqueness disappears after low-cut filtering. The filtered data allow for a wider range of possibilities of interpretation based on visual continuity in seismic events with the same waveform and energy, illustrating the higher uncertainty in the reflector definition when the seismic data lack low frequencies.

To further refine the interpretation and reduce its uncertainty, the horizon picking can be performed on impedance or relative impedance volumes. It is worth remembering that in the case of broadband data, it is possible to have fast-track inversion results for this purpose very quickly after the processed data are available (see section "Optimization of the inversion" of this paper). The inversion process itself presents the benefit of slightly extending the data bandwidth on the high-frequency side (Pendrel and Van Riel, 2000). It integrates low-frequency information from an a priori model with higher frequencies coming from the seismic data, resulting in a final model closer to the true reflectivity model of the earth. Figure 12c shows possible refining of the target bottom (purple) interpretation on the relative inversion result (the detailed

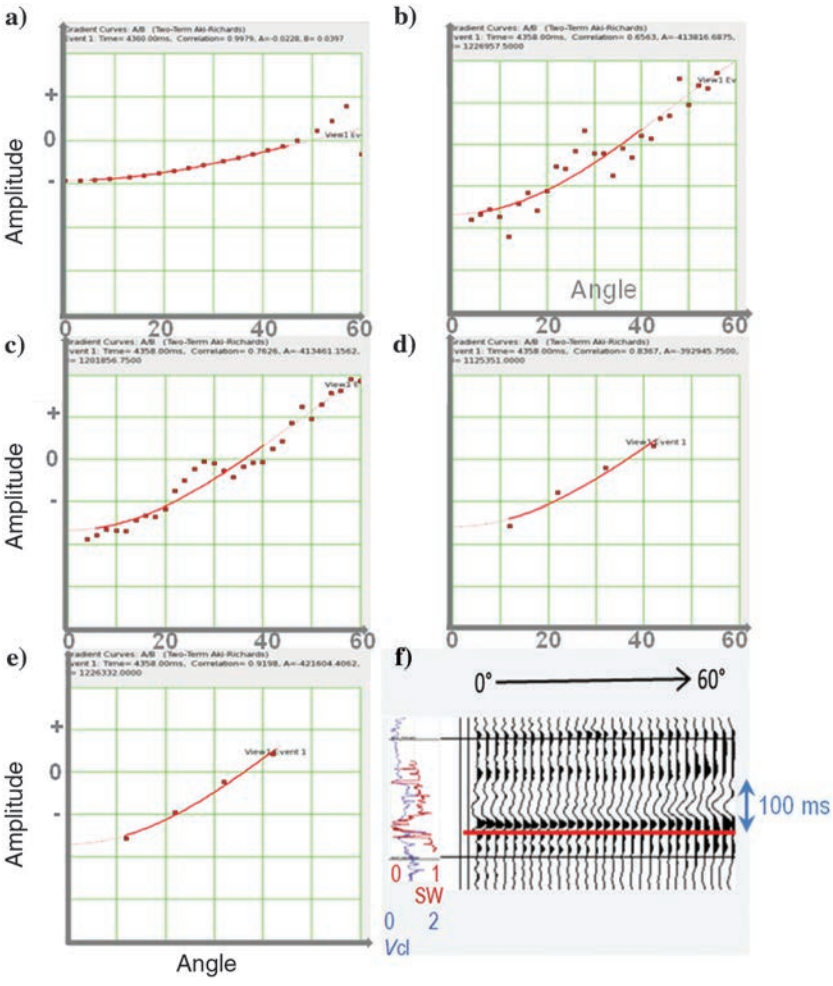

Figure 9. AVO response at well A location for (a) synthetic gather, (b) input gather, (c) after random noise attenuation, (d) after structural filter applied to angle stacks, (e) after spectral shaping, (f) input gather at the well location with Vclay and water saturation curve. Selected event corresponds to the bottom of pay zone. (b-e) The progressive decreasing dispersion of the points around the regression and preserving the AVO response that matches the synthetic response (a).

explanation of this volume calculation is presented in the inversion chapter of this work).

Another task facing the seismic interpreter is locating subtle features such as faults and fractures within the data volume. This task was significantly facilitated after the introduction of the coherency attribute by Bahorich and Farmer (1995). This attribute gives the interpreter a clear visual indication of the continuity between seismic traces. Since that time, other attributes using the same principle were developed and started to be widely used for structural interpretation.

Our area of interest is characterized by complex tectonics. To accurately define faults, we chose to calculate a coherency class attribute called horizon edge stacking. This attribute works well even on volumes with steeply dipping events, and, with further data preconditioning, it is suitable for subsequent automatic fault tracking (more details can be found in Dorn et al., 2012). Figure 13a shows a time slice of this attribute calculated from the input broadband seismic stack — the attribute clearly identifies the discontinuities present in seismic events which can be interpreted as faults. The same time slice has been extracted from the seismic data without low frequencies (after low-cut filtering, as shown in Figure 13b). Both clearly highlight discontinuities in the eastern part of the map, where the aligned areas of high attribute values (black) are located in the middle of the area with low-background values (white). Those discontinuities cutting through more continuous reflection zones can be directly interpreted as faults, and they are also seen in the seismic section view. In the central part of the time slices, the seismic reflections contain multiple small-scale discontinuities together with large-scale faults. In the absence of low frequencies, these two types of discontinuities are mixed in the attribute map into an uninterpretable product (Figure 13b). We interpret the better delineation of the faults in the broadband data as being due to the information contained in low frequencies: The full bandwidth makes it possible to better highlight the large-scale faults in zones with small-scale discontinuities. As near-vertical events with low apparent frequency, their energy is concentrated in the lower frequencies. This can also be observed from the sections in Figure 13: The section view of full-bandwidth data contains distinct faults which appear as low-frequency reflections and do not stand out as clearly after the low frequencies in the data have been filtered out.

Wavelet estimation

Wavelet estimation is a critical step for seismic reservoir characterization workflows because it creates the bridge between seismic reflections and the reflectivity series. Properly estimated amplitude and phase spectra of the operators that match seismic and log data

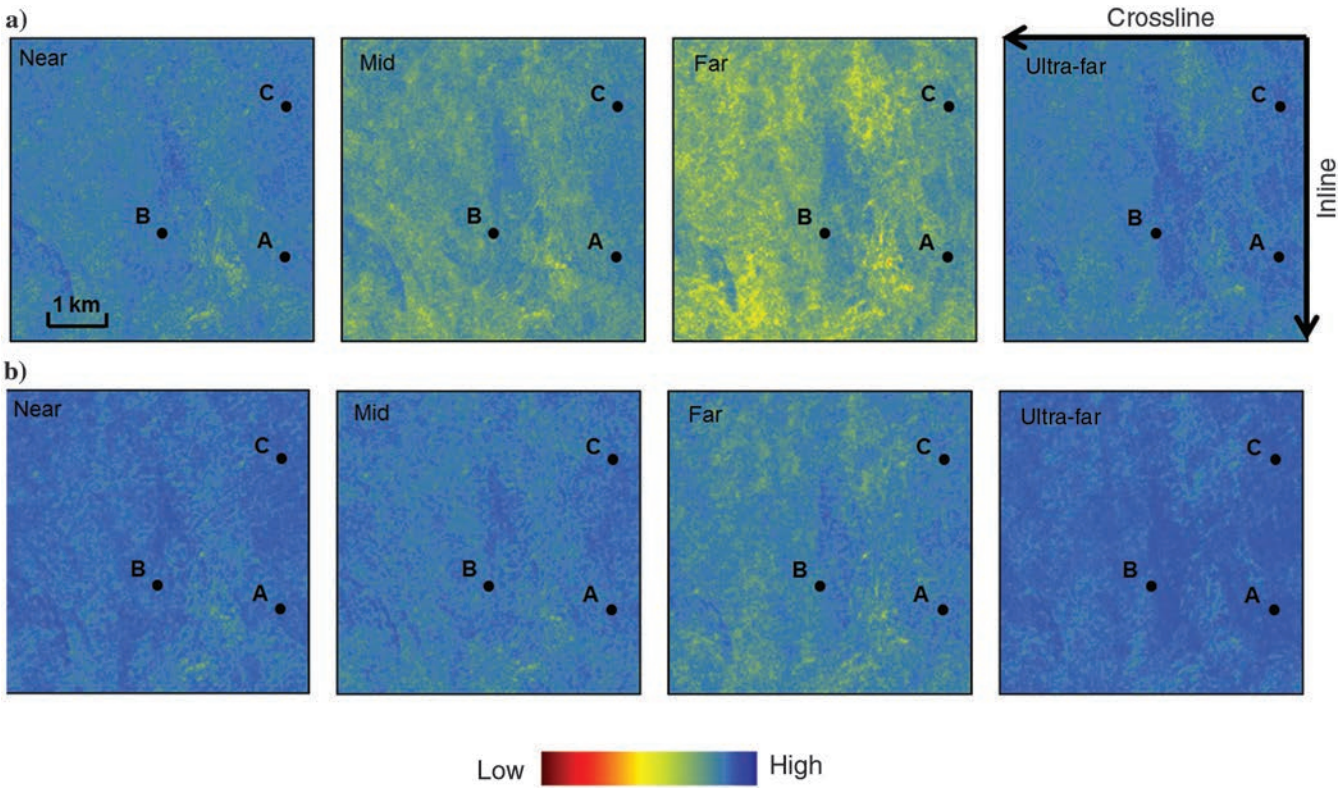

Figure 10. Quality attribute (Coleou et al., 2013) maps calculated in a 400 ms window at the reservoir level for each angle stack. (a) Raw angle stacks. (b) Final preconditioned angle stacks showing a shift to higher quality values and, therefore, a better match with the AVO model.

are key to successful acoustic and elastic inversions. We can define two main approaches for wavelet estimation — statistical and deterministic. The statistical method uses only seismic data, whereas the deterministic method uses well log reflectivity (reflection coefficients calculated from P-sonic, S-sonic, and density logs using the Zoeppritz equations) with seismic data.

We performed the wavelet estimation in the Xelerete test area in three steps, which can be summarized as (1) statistical zero-phase wavelet estimation, followed by (2) full-phase wavelet estimation at the wells only, and finally (3) a low-frequency phase estimation. We will discuss these methods in more detail.

Step 1 — Statistical zero-phase wavelet estimation: The global initial zero-phase wavelet has an amplitude spectrum based on the autocorrelation of the seismic traces. The statistical wavelet for broadband data should be estimated in a time window that is long enough to cover frequencies as low as possible with the S/N ratio of the processed data — a 1000 ms window was chosen in this case.

Step 2 — Deterministic wavelet estimation at well locations, using the crosscorrelation between synthetic and seismic traces in the target interval and the statistical wavelet as additional input information. The statistical wavelet estimated in step 1 contains the global amplitude spectrum of the data in the selected interval and is used to create synthetic traces using the convolutional model (Edgar and van der Baan, 2011). Altering the phase and amplitude spectra of the wavelet to reach the maximum crosscorrelation between the synthetic and seismic traces, we estimate the deterministic wavelet at well locations. This wavelet contains the part of the data spectrum which matches the well reflectivity or, in other words, the part of the data spectrum containing geologic information. The deterministic wavelet extraction allows for a robust estimation of the phase and amplitude spectra of the operator at well locations when log data are available, presenting a reasonable well-to-seismic tie characterized by the high crosscorrelation between seismic and well synthetic data, over a sufficient time gate. As a general guideline, the extent in time of the well logs should be 2–3 times the wavelet length to obtain a stable estimation of the operator.

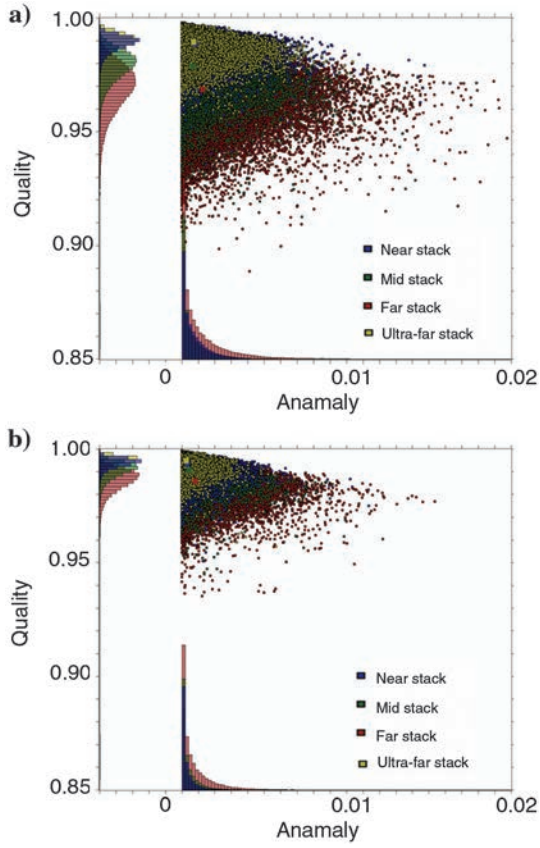

Figure 11. Quality and anomaly attributes (Coleou et al., 2013) calculated in a 400 ms window at reservoir level and displayed in a crossplot where each point represents a bin in the survey. (a) Raw angle stacks. (b) Final preconditioned angle stacks, showing an overall shift to higher values of quality and lower anomaly values, indicating a better fit with the AVO model.

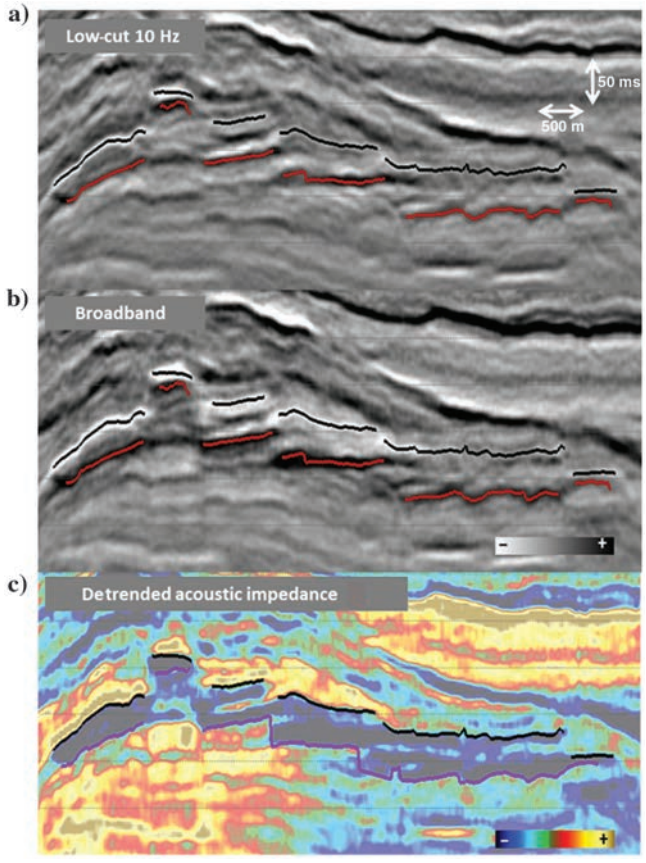

Figure 12. Section view with top and base of the interval of interest interpreted: (a) on seismic data without low frequencies (low-cut filter 10 Hz applied), (b) on full-bandwidth broadband seismic data, and (c) on a detrended acoustic impedance section (relative impedance values). It is easier to pick the events on the full-bandwidth data due to the sharper wavelet with reduced side lobes, but the impedance section provides the clearest demarcation of the interval of interest.

Figure 14 shows the calibrations of wells A and B with the full seismic stack and the deterministic wavelets extracted from these wells. The estimation at well A was performed in a 400 ms time window, and the crosscorrelation graph has a well-defined maximum at the value 0.91. The wavelet estimation in well B was performed in a 300 ms time window with a crosscorrelation of 0.81. The objective of the study is to identify the oil sand, which can be identified by low values of SW (water saturation) log in Figure 14. The amplitude and phase spectra of the deterministic operators are shown in Figure 15. The wavelet estimated in well B displays a lower phase stability, especially for high frequencies, and a lack of low-frequency energy compared with the wavelet estimated in well A. This lateral variability in the energy concentrated at low frequencies, which we observe between wells A and B (Figure 15), was confirmed by an extended lateral analysis: Figure 16a contains the map of seismic energy corresponding to the signal at 5 Hz in a time window of 600 ms around the reservoir calculated for the full stack. We observe that, for these low frequencies, the energy of the seismic data is highly variable, and the difference in signal content observed at the wells is not a localized phenomenon. When compared with other QC done on the full-bandwidth full stack, these features are observable on other attributes such as the dominant frequency, bandwidth, or rms of the amplitudes (Figure 16b–16d), confirming that the trend of low frequencies can be related to geology.

After analysis of the deterministic wavelets at each well, and to obtain optimal wavelets for acoustic and elastic inversions, the wavelet extraction is performed

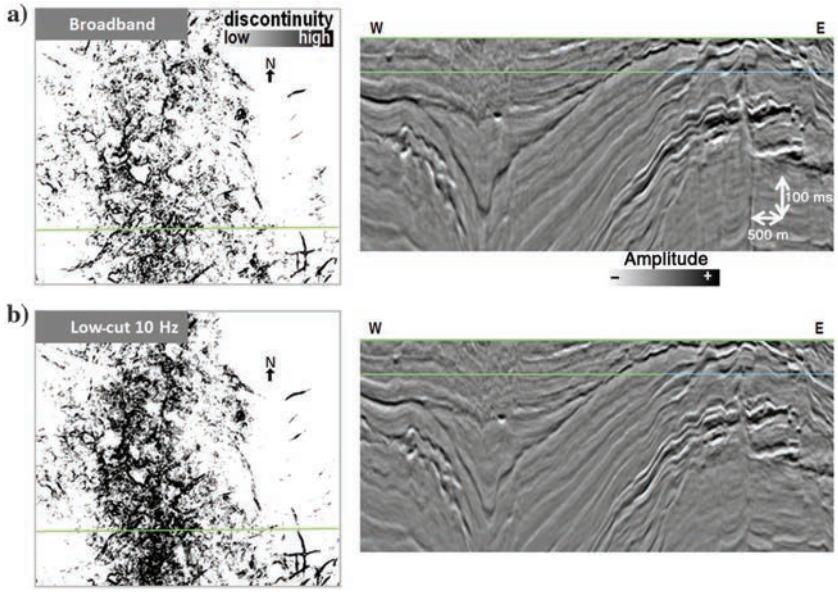

Figure 13. Horizon edge attribute time slice and corresponding vertical sections for (a) full-bandwidth broadband seismic stack and (b) 10 Hz low-cut filtered seismic stack. The full-bandwidth images provide a sharper image of the faults and a cleaner discontinuity attribute map.

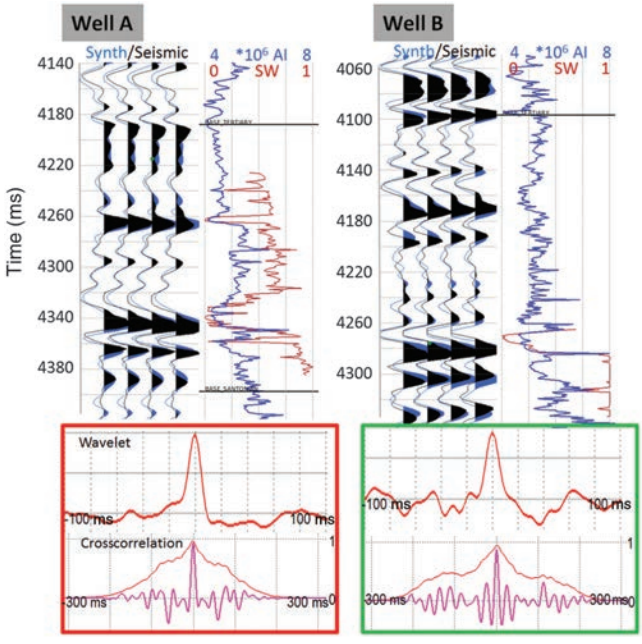

Figure 14. Well-to-seismic tie panel for two wells: well A and well B with the corresponding wavelets estimated and crosscorrelation functions between synthetic (blue) and seismic (black) traces. The wavelet estimated in well B displays lower phase stability, especially for high frequencies, and a lack of low-frequency energy compared with the wavelet estimated in well A.

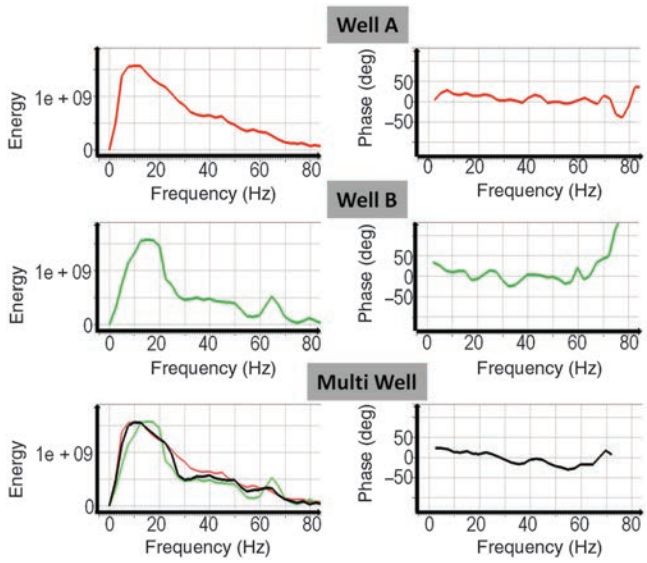

Figure 15. Amplitude and phase spectra of wavelets extracted in well A, well B, and multiwell wavelet extraction which maximizes the crosscorrelation function calculated in wells A and B simultaneously.

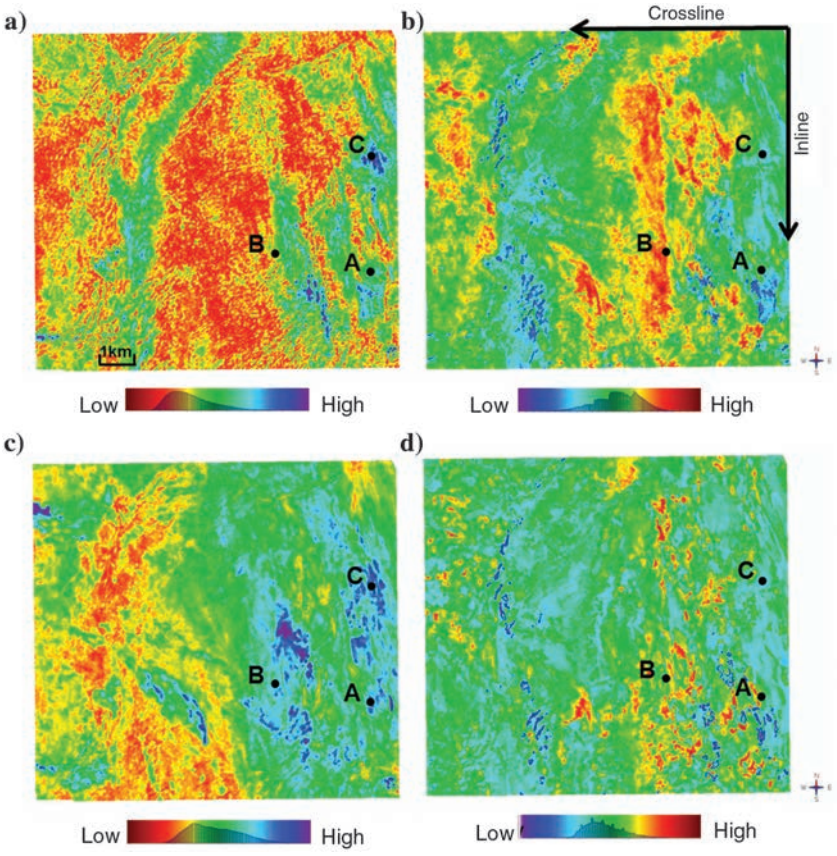

Figure 16. (a) Spectral decomposition result. Map of the energy corresponding to the signal of 5 Hz in the full stack. (b) Dominant frequency of the full stack. (c) Root-mean-square energy of the full-stack full bandwidth. (d) Bandwidth of the full stack. This frequency attribute analysis was performed jointly with the final wavelet estimation and is crucial to avoid missing the low frequencies in the final wavelet. The maps indicate that well C is in an area where the seismic has limited bandwidth.

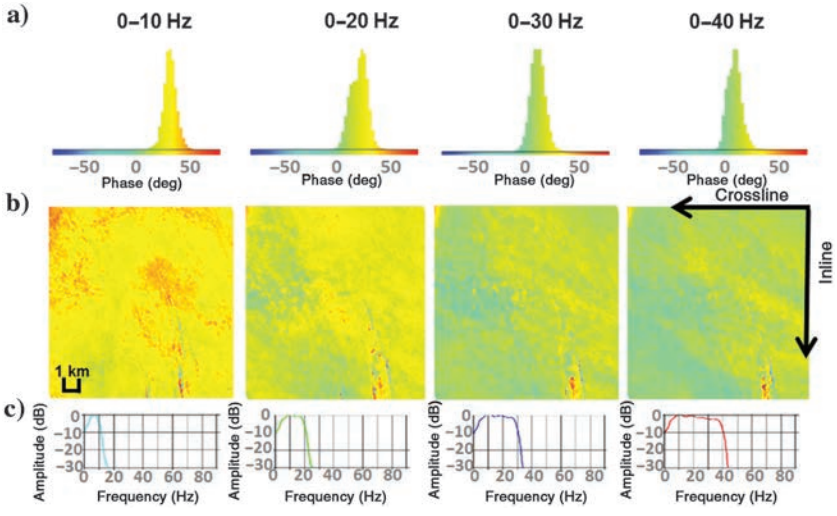

Figure 17. Phase estimation using the maximum kurtosis method for different bandwidths. (a) Phase histograms, (b) phase maps, and (c) the spectra for the different frequency bands.

using several wells simultaneously. The process is called multiwell wavelet extraction and estimates the wavelet that maximizes a crosscorrelation function calculated in several wells simultaneously. The "best" wells with reliable calibration are chosen to be used in this kind of wavelet extraction — wells A and B in our case. Well C is not used due to it having the lowest crosscorrelation coefficient and will only be used for additional QC as a blind well.

When a multiwell wavelet is extracted (Figure 15), it repeats the shape of the wavelet "richest" in low frequencies, extracted in well A. For the high frequencies, the multiwell wavelet follows the poorest well wavelet. It is an important fact to consider in the case where we have well data in an area with poor low-frequency content. The frequency map analysis (Figure 16) performed jointly with the final wavelet estimation is crucial to avoid missing those low frequencies in the final wavelet. If this range of frequencies was not represented in the operator, it would prevent the inversion from properly recovering the corresponding signal, missing out on one of the main benefits of broadband data for the inversion process. The multiwell wavelet is reliable for mid and high frequencies, but the phase estimation in low frequencies (the first 10 Hz) requires additional analysis, which is explained here as step 3 in our wavelet estimation flow for broadband data.

Step 3 — Phase estimation for the low frequencies was performed using three alternative methods: (1) phase extrapolation from mid toward low frequencies as shown by Schakel and Mesdag (2014), (2) maximum kurtosis determination, and (3) wavelet estimation in wells A and C that have the longest interval of logs in the time domain.

Schakel and Mesdag (2014) suggest that the phase of the broadband data at low frequencies follows a linear trend rather than being of a constant value in this range, and they introduce a practical approach to broadband wavelet estimation. The phase of the multiwell wavelet shown in Figure 15 is extrapolated toward low frequencies following this first phase estimation method, applied in this case for frequencies of less than 7 Hz. Indeed, none of the wells shows a reliable well-to-seismic tie in a time window

greater than 400 ms. When trying to increase the time gate used for the match, we observe a drop in crosscorrelation that does not allow us to have confidence in the resulting wavelet.

The maximum kurtosis method is based on the fact that seismic reflectivity sequences have amplitude distributions that are leptokurtic, that is to say, they are more heavy-tailed than a Gaussian distribution (White, 1988). This method estimates a constant phase shift over the input bandwidth. This method is sensitive to the amount of data used in the estimation in relation to this threshold. The phase estimation was performed using four different bandwidths: 0–10 Hz, 0–20 Hz, 0–30 Hz, and 0–40 Hz in a 2 s time window. Figure 17 shows the maps of the obtained phase shifts (deviation from zero phase) for each frequency range. The tendency of phase values to increase toward the lowest frequencies is in accordance with what was seen in the multiwell wavelet (Figure 15).

Two of the wells located in the area (wells A and C) have representative intervals of sonic and density logs available. However, neither of these wells have a reliable well-to-full bandwidth seismic tie for the whole interval of logs. Therefore, the wavelets shown in Figures 14 and 15 were estimated in the reservoir interval only. But the complete time interval of available log data was used in these wells to run a comparative estimate of the phase for the low frequencies between 0 and 10 Hz. Figure 18 shows the calibration of wells A and C to the low-frequency part of the seismic: 0–10 Hz. Well A was calibrated with low-pass-filtered seismic in a 0.9 s long interval with crosscorrelation of 0.85, and well C was calibrated in a 0.8 s long interval with a crosscorrelation of 0.93.

The results of the three independent methods of low-frequency phase evaluation are compiled in Figure 19: the statistical maximum kurtosis method, the deterministic method through calibration of wells to the low-frequency part of the seismic, and an empirical approach proposed by Schakel and Mesdag (2014) to follow the linear trend extrapolating phases from mid to low frequencies. All methods delivered consistent results, and the multiwell wave-

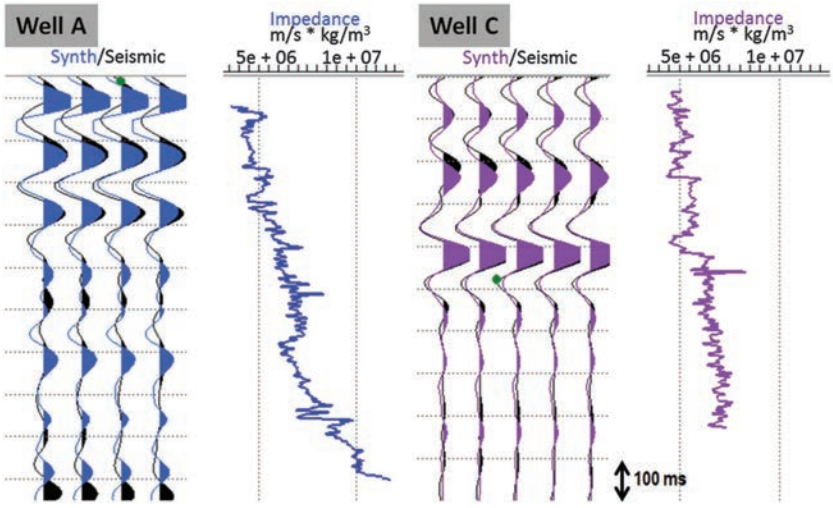

Figure 18. Calibration of seismic to well log synthetics at wells A and C using the low-frequency part of the seismic (0–10 Hz) helps decrease the uncertainty in phase estimation for low frequencies.

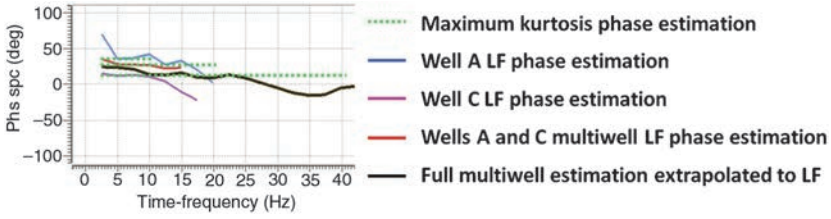

Figure 19. Phase estimated for low frequencies using three different methods. All methods delivered consistent results, and the uncertainty of the wavelet phase estimation at low frequencies can be inferred from the spread observed between the different methods and the multiwell wavelet.

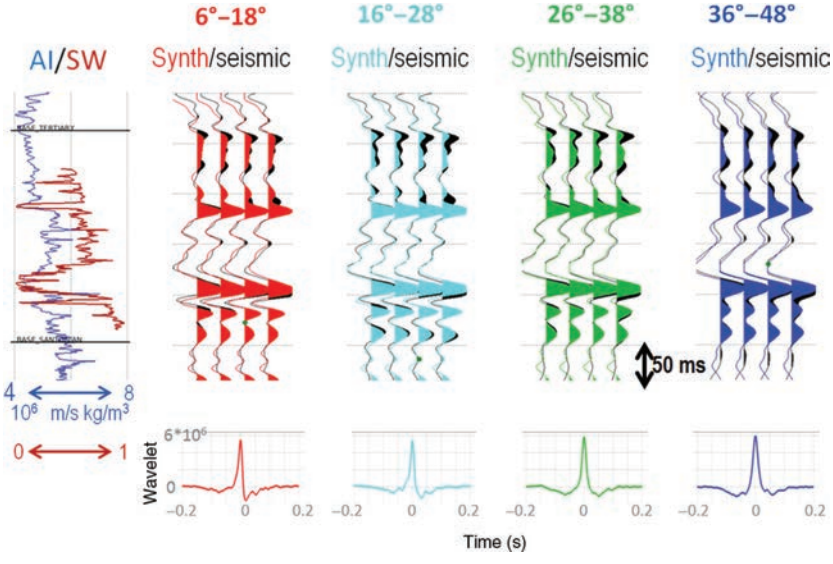

Figure 20. Calibration of angle stacks with well A well log synthetics and corresponding wavelets extracted for use in the elastic inversion. AI, acoustic impedance curve; SW, water saturation curve in well A.

let with the phase shown as a black line in Figure 19 was used in the following inversion. The uncertainty of the wavelet phase estimation at low frequencies can be inferred from the spread observed between the different methods tested here: approximately ±15° around the multiwell wavelet at 5 Hz.

To extract wavelets for the elastic inversion, the same methodology was used to extract angle-dependent wavelets for near, mid, far, and ultra-far angle stack — the result is illustrated in Figure 20. Note that in the elastic case, only well A had adequate logs to perform the deterministic wavelet extraction, and the other wells do not have measured V_S logs.

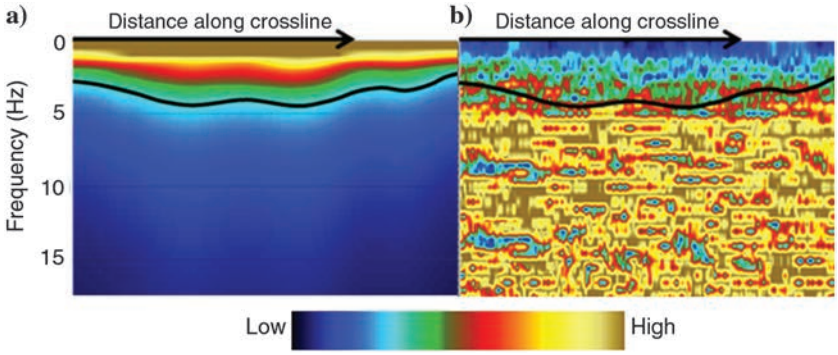

Figure 21. Crossline 6280 — time-frequency display of the energy of (a) initial acoustic impedance initial model derived from seismic velocities and (b) full-bandwidth seismic stack. Significant overlap around an average frequency of 3.5 Hz can be observed, confirming that no additional information is required to recover a complete frequency bandwidth during the inversion.

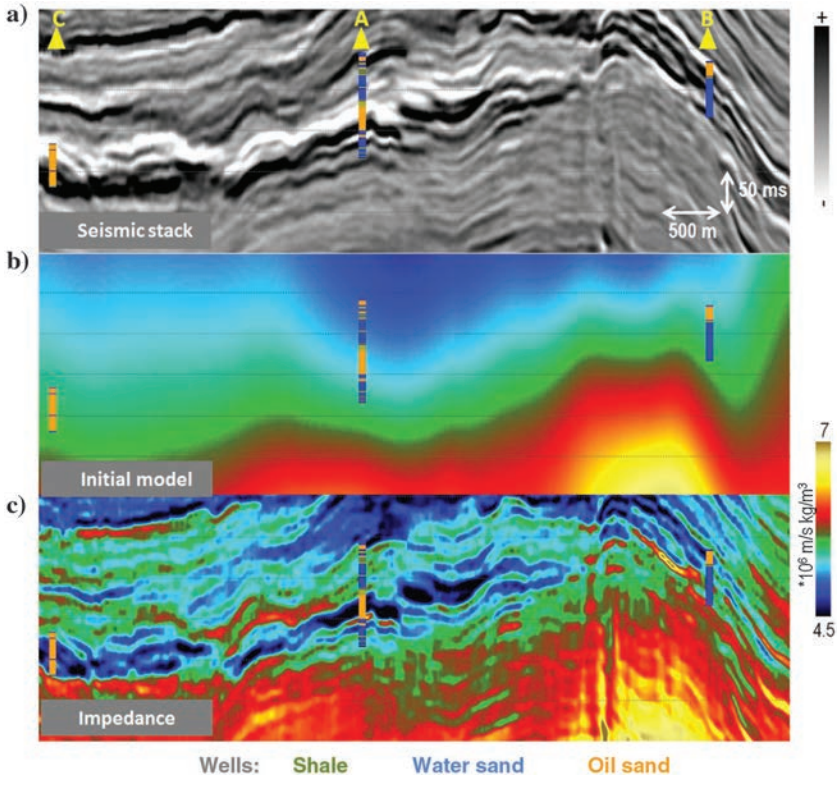

Figure 22. Random line through three wells. (a) Seismic stack, (b) initial model, and (c) acoustic inversion result. Well lithology logs are superimposed on the inversion results. The oil sand lithology can be seen to match zones of low acoustic impedance as expected.

Optimization of the inversion

In accordance with the rock-physics analysis presented in the case study overview, two deterministic inversions were performed sequentially with the corresponding facies classification: poststack- and prestack-constrained sparse-spike inversions.

A poststack or acoustic-constrained sparse-spike inversion creates an acoustic impedance model from the seismic reflection data. The P-impedance is estimated by minimizing an objective function that contains multiple terms: residuals (the mismatch between seismic and synthetic), a contrast misfit (controls sparseness), a trend misfit (the difference between the final result and the initial impedance model), and a soft spatial misfit (controls the lateral smoothness of the result).

Deterministic inversion requires a low-frequency model to bring into the inversion result the low-frequency information that is missing in seismic data. The frequency bandwidth of this initial model depends on the lowest usable frequency (in terms of the S/N) of the seismic data spectra. A wide gap of missing low frequencies (e.g., 0–10 Hz typically for conventional seismic data) will require building a detailed initial model. The narrower the gap of absent seismic frequencies, the more data driven the inversion is. Initial models for conventional seismic data are usually obtained from low-pass-filtered elastic attributes logs at the well locations, followed by an interpolation method (kriging for instance). This method of model building requires stratigraphic model (framework) to perform interpolation inside it. This stage of the inversion workflow brings significant uncertainty to the inversion as the low-frequency model created through log interpolation is conditioned by the number of wells in the area, the reliability of the stratigraphic model used in the interpolation and extrapolation of the sparse impedances, and lateral variability in elastic properties (Pendrel and Van Riel, 2000).

Seismic data acquired using variable-depth streamers are ideally suited for inversion because they provide more of these missing low frequencies (typically down to 3 Hz), hence decreasing the

dependence on well data to build the inversion low-frequency initial models, which would now only need to have a bandwidth of 0–4 Hz). The initial model created directly from seismic velocity without use of a stratigraphic model and seismic logs was used in our case. Because the trace-based inversion algorithm was used (not stratigraphic inversion), the structural framework was not necessary to perform inversion. Figure 21 illustrates the time-frequency information contained in 1) the acoustic impedance initial model calculated from seismic velocities and density calculated from a sonic-density relationship derived at the well and 2) the seismic full stack. Significant overlap around an average frequency of 3.5 Hz can be observed, confirming that no additional information is required to recover a complete frequency bandwidth during the inversion.

Figure 22a–22c shows an acoustic inversion plot including seismic stack, initial model, and impedance obtained from the acoustic inversion result. Figure 23 shows the QC of acoustic inversion results at the wells, comparing the impedance values of well logs and inverted values along wells. Because no well interpolation was used in the low-frequency model construction, the results are the direct consequence of the calibration of the seismic velocity model and seismic amplitudes. This plot demonstrates the good match between the final inversion results and the measured data from wells, confirming the possibility to further use the inversion results for qualitative and quantitative interpretation. Considering the low level of vertical details introduced by the initial model (Figure 22b), the good match observed is due to the information derived from the broadband seismic data (and the low frequencies in particular). We calculated the frequency-domain normalized root-mean-square (fNrms) difference between real data and inversion synthetic data. This attribute, displayed in Figure 24 for crossline 6280 that runs close to wells A and C, is useful to assess the quality of the match between inverted synthetic and real data as a function of frequency. We can observe in our case that information is contained in the broadband data over a large range of frequencies from 3.5 to 55 Hz. The match then degrades toward frequencies of 70 Hz where no valuable information is retrieved by the inversion process.

Prestack or elastic-constrained sparse-spike inversion creates a set of elastic models by simultaneously inverting multiple seismic partial (angle or offset) stacks. In our case, and following the results from the initial rock-physics analysis, the acoustic (I_P) and shear (I_S) impedance volumes obtained from the inversion were used to calculate the Lamé impedances lambda-rho and mu-rho.

Figure 25 shows a section view of these parameters after applying detrending, and Figure 26 presents the QC at well A comparing measured values from the well logs to the inverted values.

A good match at the wells was observed for the acoustic and elastic inversion results from the broadband data (Figures 23 and 26). The initial model for inversion (Figure 22b) was created directly from the

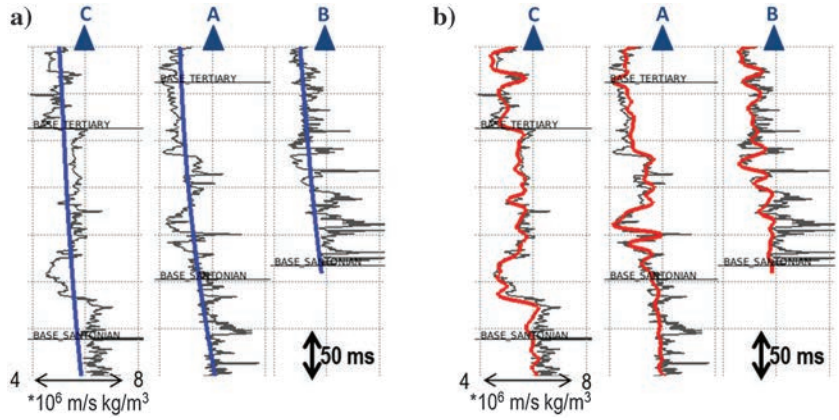

Figure 23. Well QC of acoustic inversion. Black, acoustic impedance values from well logs; (a) blue, acoustic impedance initial model; and (b) red, inverted acoustic impedance. This demonstrates the good match between the final inversion results and the measured data from wells, confirming the possibility to further use the inversion results for qualitative and quantitative interpretation.

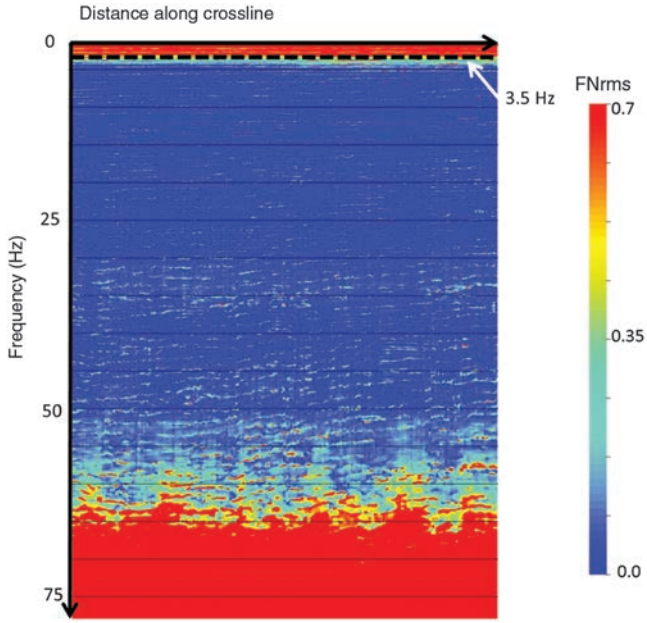

Figure 24. The fNrms (the difference between inverted real and synthetic data for crossline 6280). We can observe a good match from 3.5 to 55 Hz. The match then degrades toward frequencies of 70 Hz where no valuable information is retrieved by the inversion process.

seismic velocity without any use of filtered well data and interpolation models. Thus, no horizon interpretations were necessary to create the initial model. This makes broadband data inversion more data driven than the conventional seismic data inversion, where the intervention of geophysicists has a much bigger impact on the result through the building of a more detailed initial model. It also speeds up the inversion workflow, making it possible to achieve fast-track inversion results very quickly after the final processed seismic data become available and therefore providing better information earlier in the workflow to support drilling decisions.

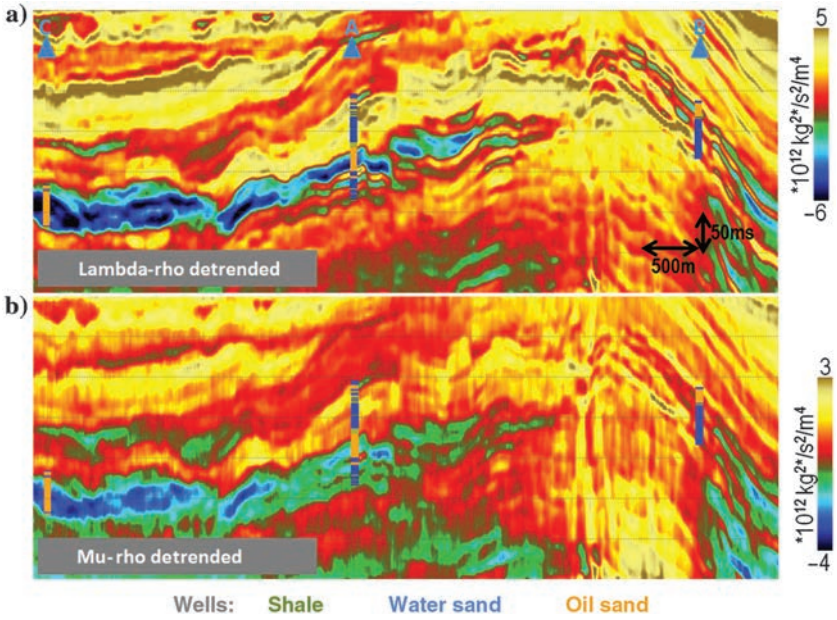

Figure 25. Elastic inversion result after detrending. (a) Lambda-rho and (b) mu-rho. Detrending of the elastic properties from inversion provides a better separation of the lithoclasses for interpretation.

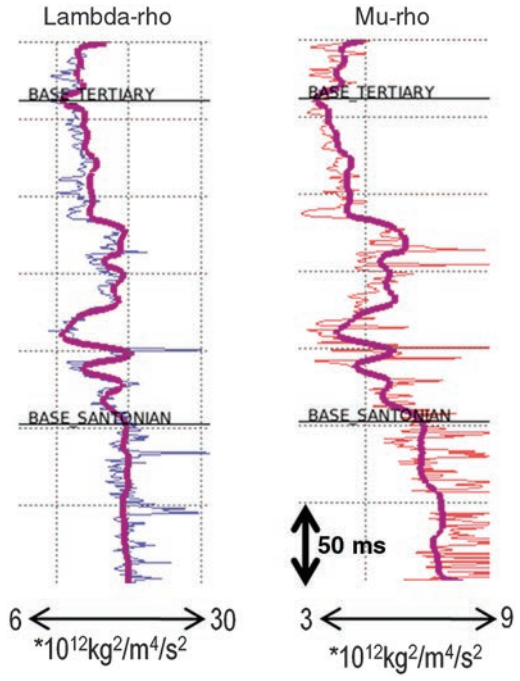

Figure 26. QC of elastic inversion in well A. Blue curve, lambda-rho calculated from well logs in well A; red curve, mu-rho calculated in well A; and purple curves, the corresponding estimates from the inversion, which indicate a good match with the well data.

Lithofacies definition and classification

With the results obtained from the acoustic and elastic inversions, deterministic and probabilistic interpretations were performed to localize the reservoir pay zone.

Deterministic interpretation was performed by application of a cutoff on the inverted properties, as defined in Figure 5 for acoustic impedance values. This result is shown in Figure 27a. This zone matches with the pay zone in the wells (orange), but the main limitation of this approach is the absence of information regarding the uncertainty related to the classification. The ranges of facies values we aim to identify (via acoustic impedance or lambda-rho and mu-rho in our case) show significant overlap with the other facies defined at the wells. No related information is taken into account when using a simple threshold for defining limits between lithoclasses, whereas the uncertainty of the classification will directly result from the degree of overlap.

A more robust probabilistic approach was undertaken through the application of a supervised Bayesian classification technique to infer the probability of predefined lithofacies from the inversion results (Mukerji et al., 2001, Pendrel et al., 2006). To characterize the pay zone, the three lithofacies (shale, water sands, and oil sands) were first defined from well log information such as porosity and saturations. The method then requires the creation of probability density functions for each facies, which determines the probability that a particular combination of elastic parameter values represents a given facies. This was done by creating a histogram for acoustic inversion or a crossplot of the elastic parameter curves (color coded by the facies in Figure 28) and fitting a probability density function (PDF) to the samples associated with each of the facies. A prior probability of each facies can be estimated, indicating the relative proportion of each facies that is expected within the region of interest, or, as it was done in our case — assuming that the a priori probabilities equal: 33.3% — shale, 33.3% — oil sand, and 33.3% —

water sand. These facies-conditioned PDFs and a priori geological information are then combined within a Bayesian inference framework to generate facies probability volumes from the inverted elastic parameter volumes. PDFs were built using log information resampled to 4 ms sample rate in time domain, same as seismic sample rate. Figure 28a shows the PDFs established using detrended impedance logs in wells A, B, and C. These PDFs were applied to our acoustic inversion result and give the pay probability volume shown in Figure 27b. Figure 28b shows the PDFs established for the detrended lambda-rho–mu-rho pair of parameters, and Figure 27c represents the result of facies classification using the elastic inversion result.

Comparing the classifications of the elastic (Figure 27c) and acoustic (Figure 27b) inversions, a large reduction in the predicted oil sands zone is observed. The oil sands probabilities at the wells in the elastic and acoustic cases are shown in Figure 29 and are compared with the water saturation logs. Although the prediction of the pay zone at the wells still matches with log data, much of the predicted oil sandstones obtained in the acoustic case is no longer present in the classification from the elastic case. The classification performed using acoustic inversion results tends to overestimate the amount of oil sands, whereas switching to the elastic domain results in a more conservative prediction of the pay zone in the area.

The benefits of broadband data for inversion and facies classification have been previously illustrated, in particular, by demonstrating the uplift brought by the low frequencies in recovering the absolute values of elastic properties and subsequent reservoir delineation, in particular in the case of thick reservoirs (Lafet et al., 2012). In the inversion process, using broadband data results in more seismic-driven inverted property volumes. The final results are less dependent on the initial model building, which can often be a major source of uncertainty. Another aspect worth mentioning is the fact that, within the seismic bandwidth, a better separation of the facies is achieved when low frequencies are present. We illustrate this aspect by showing the training sets obtained by crossplotting lambda-rho and mu-rho from wells applying 2 and 10 Hz low-cut filters (Figure 30). The amount of overlap between facies (and therefore of uncertainty in the classification) is significantly increased when the lower frequencies are filtered out.

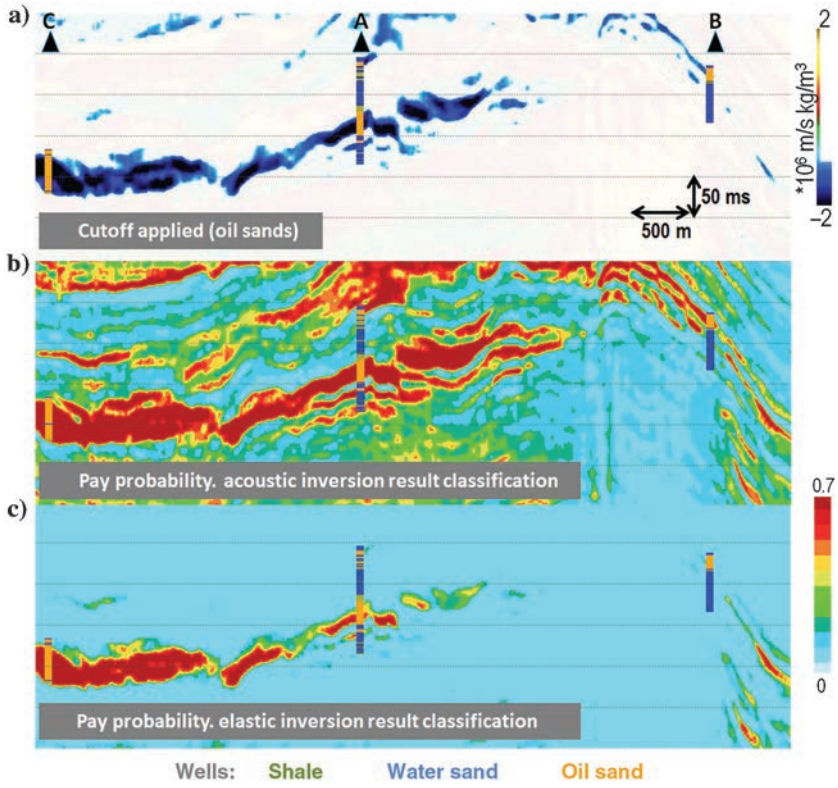

Figure 27. Interpretation of inversion results with well lithology logs superimposed: (a) Detrended acoustic impedance with cutoff threshold applied to separate the oil-saturated sandstone. (b) Pay probability obtained through Bayesian classification of detrended acoustic inversion result (c) Pay probability obtained through Bayesian classification of detrended elastic inversion result. The elastic inversion pay probability provides a much more conservative interpretation of oil sand distribution.

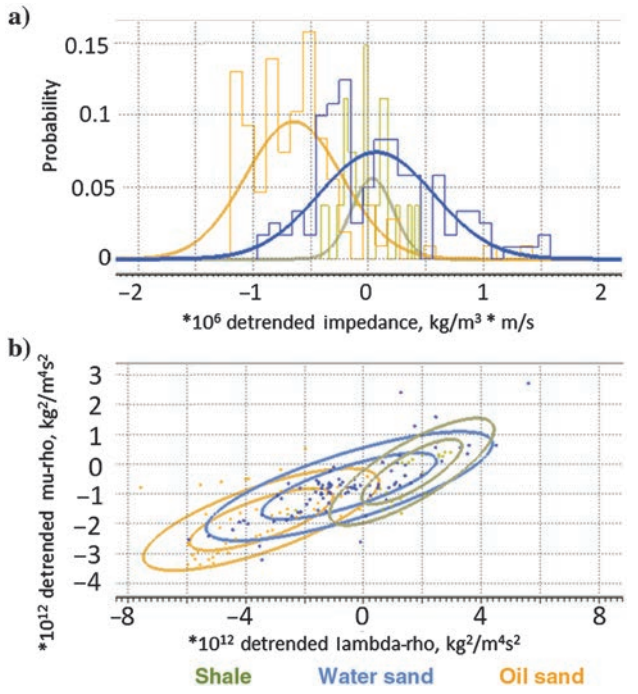

Figure 28. The PDFs used to perform the Bayesian lithoclassification. (a) Detrended acoustic inversion PDFs and (b) detrended elastic inversion PDFs.

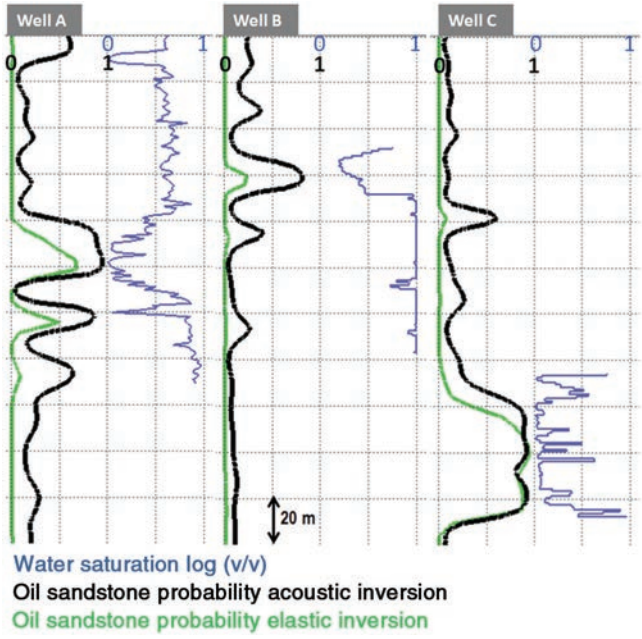

Figure 29. Lithofacies Bayesian classification at the wells from acoustic and elastic inversions, compared with the water saturation logs. The acoustic inversion lithology prediction tends to overestimate the amount of oil sands in this case, but it includes all the pay zones (low water saturation). The elastic inversion lithology prediction results in a more conservative prediction of the pay zone in this case.

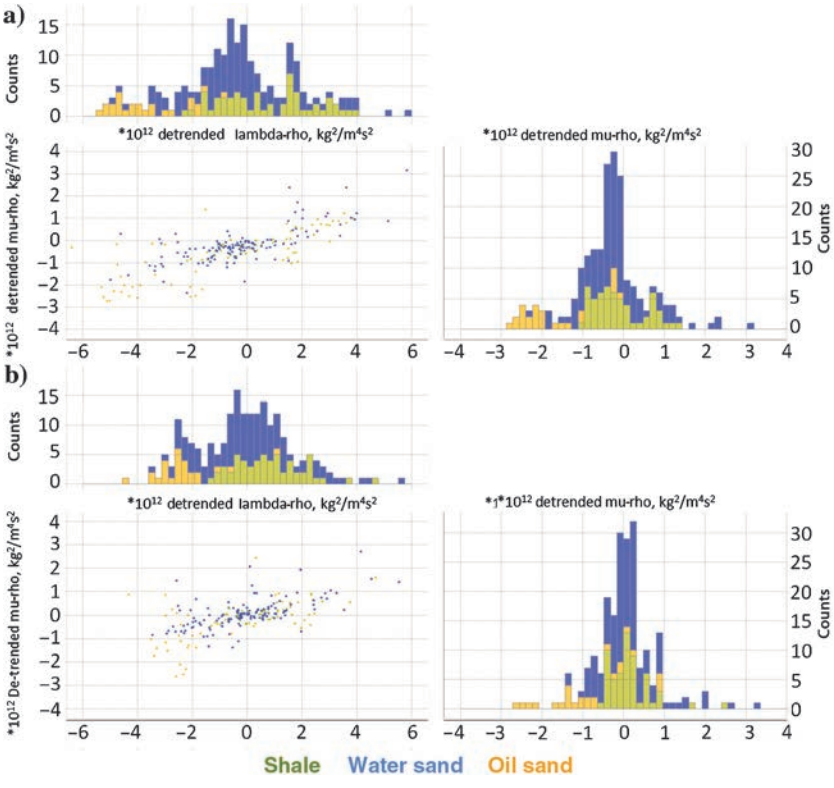

Figure 30. Lambda-rho–mu-rho crossplots from well A logs and associated histograms for each axis, colored by seismic facies: (a) after 2 Hz low-cut filter application and (b) after 10 Hz low-cut filter application. The amount of overlap between facies (and, therefore, the uncertainty in the classification) is significantly increased when the lower frequencies are filtered out.

Conclusion

Following the acquisition of a variable-depth streamer survey by CGG in 2014 and the processing of the seismic data, a specifically adapted broadband seismic reservoir characterization workflow (including data preconditioning, structural interpretation, wavelet estimation, seismic inversion, and facies classification) was performed to characterize the extent of the oil-bearing Santonian sandstones identified at three exploration wells. These steps should contribute to a better understanding of the geology in the area, ultimately leading to the building of a reliable reservoir model populated with realistic properties.

We showed a seismic data imaging flow that uses sparse log data for local QC around the wells and global, horizon-based QC attributes elsewhere. We illustrated the potential difficulties and particular care that should be taken when dealing with broadband data, and we showed in which aspects it can provide additional value to the interpreter compared with conventional data. Lithofacies classification cubes of the target pay zone have been computed from this workflow, showing a good match with observations at the wells and along with a quantification of the uncertainty inherent in the classification method.

Several aspects of this work suggest that the benefits of broadband data observed when running deterministic inversion should extend to more advanced inversion processes. In particular, we showed how broadband data also benefit the structural interpretation (geology), geometric attributes, and PDF construction aspects, all of which can be integrated into a stochastic inversion workflow. A natural extension to this work would therefore be to further explore how broadband data can be used as an input to geostatistical workflows.

Acknowledgments

The authors would like to thank CGG Multi-Client & New Ventures for sharing their data and good dialog during the project, as well as for their permission to publish this work. We would also like to thank R. Taylor, H. Hoeber, and R. Porjesz for their feedback and constructive discussions.

References

Alves Marcos Andre Alves, 2007, Brazil Round 9: ANP.

Araman, A., and B. Paternoster, 2014, Seismic quality monitoring during processing: First Break, **32**, 69–78.

Bahorich, M. S., and S. L. Farmer, 1995, 3-D seismic discontinuity for faults

and stratigraphic features: The Leading Edge, **14**, 1053–1058, doi: 10.1190/1.1437077.
Bastos, G., 2015, Agência nacional do petróleo, gás natural e biocombustíveis. décima terceira rodada de licitações. bacia de campos. Sumário Geológico e Setores em Oferta.
Coleou, T., J. P. Coulon, D. Carotti, P. Dépré, G. Robinson, and E. Hudgens, 2013, AVO QC during processing: 75th Annual International Conference and Exhibition, EAGE, Extended Abstracts, doi: 10.3997/2214-4609.20130875.
Dorn, G. A., P. E. Murtha, and B. Kadlec, 2012, Imaging faults in 3D seismic volumes: 82nd Annual International Meeting, SEG, Expanded Abstracts, doi: 10.1190/segam2012-1538.1.
Duval, G., 2012, How broadband can unlock the remaining hydrocarbon potential of the North Sea: First Break, **30**, 85–91.
Edgar, J., and M. van der Baan, 2011, How reliable is statistical wavelet estimation?: Geophysics, **76**, no. 4, V59–V68, doi: 10.1190/1.3587220.
Goodway, W., 2001, AVO and Lame's constants for rock parameterization and fluid detection: CSEG Recorder, **26**, 39–60.
Hu, B., H. Shen, P. Wang, and V. Tyagi, 2014, Premigration ghost wavefield elimination on different cable configurations — A case study in the Gulf of Mexico: 76th Annual International Conference and Exhibition, EAGE, Extended Abstracts, Tu E103 16.
Kneller, E., A. Ferrer, and J. Langlois, 2013, Benefits of broadband seismic data for reservoir characterization, Santos Basin, Brazil: 13th International Congress of the Brazilian Geophysical Society & EXPOGEF, 26–29: 966–970.
Lafet, Y., L. Michel, R. Sablon, D. Russier, and R. Hanumantha, 2012, Variable depth streamer: Benefits for rock property inversion: 75th Annual International Conference and Exhibition, EAGE, Extended Abstracts, doi: 10.2523/IPTC-16804-Abstract.
Masclet, S., C. Dolymnyj, S. Domont, F. Marpeau, and H. Douma, 2015b, Improving presalt imaging through multilayer horizon-constrained tomography — A case study in Brazil's Campos basin: 14th International Congress of the Brazilian Geophysical Society & EXPOGEF, 1032–1037, doi: 10.1190/sbgf2015-205.
Masclet, S., S. Domont, C. Dolymnyj, H. Prigent, H. Douma, M. Reinier, and M. Tanis, 2015a, The impact of broadband acquisition and processing on imaging Brazil's deep water Campos basin: 14th International Congress of the Brazilian Geophysical Society & EXPOGEF, 978–982, doi: 10.1190/sbgf2015-193.
Mesdag, P., and M. Schakel, 2015, Improving seismic reservoir characterization with broadband seismic: Offshore Technology Conference, 280–287. doi: 10.4043/25668-MS.
Michel, L., and R. Sablon, 2016, Quantitative interpretation — Broadband data uplift: 78th Annual International Conference and Exhibition, EAGE, Extended Abstracts, WS01 D01.
Mukerji, T., A. Joerstad, P. Avseth, G. Mavko, and J. R. Granli, 2001, Mapping lithofacies and pore-fluid probabilities in a North Sea reservoir: seismic inversions and statistical rock physics: Geophysics, **66**, 988–1001, doi: 10.1190/1.1487078.
Mutti, E., and M. Carminatti, 2012, Deep-water sands of the Brazilian offshore basins: Search and Discovery, Article #30219 http://www.searchanddiscovery.com/pdfz/documents/2012/30219mutti/ndx_mutti.pdf.html.
Pendrel, J., C. Mangat, and M. Feroci, 2006, Using bayesian inference to compute facies-fluid probabilities (FFP): CSPG CSEG CWLS Convention, 278.
Pendrel, J., and P. Van Riel, 2000, Effect of well control on constrained sparse spike seismic inversion: CSEG Recorder, **25**.
Reiser, C., T. Bird, F. Engelmark, E. Anderson, and Y. Balabekov, 2012, Value of broadband seismic for interpretation, reservoir characterization and quantitative interpretation workflows: First Break, **30**, 67–75.
Schakel, M. D., and P. R. Mesdag, 2014, Fully data-driven quantitative reservoir characterization by broadband seismic: 84th Annual International Meeting, SEG, Expanded Abstracts, 2502–2506.
Soubaras, R., 2016, Prestack wavelet estimation for broadband data: 86th Annual International Meeting, SEG, Expanded Abstracts, 3636–3640.
Soubaras, R., R. Dowle, and R. Sablon, 2012, BroadSeis: Enhancing interpretation and inversion with broadband marine seismic: CSEG Recorder, **37**, 40–46.
Soubaras, R., and P. Whiting, 2011, Variable depth streamer — The new broadband acquisition system: 81st Annual International Meeting, SEG, Expanded Abstracts, 4349–4353.
Wallick, B. P., and L. Giroldi, 2013, Interpretation of full-azimuth broadband land data from Saudi Arabia and implications for improved inversion, reservoir characterization, and exploration: Interpretation, **1**, T167–T176, doi: 10.1190/INT-2013-0065.1.
White, R. E., 1988, Maximum kurtosis phase correction: Geophysical Journal, **95**, 371–389, doi: 10.1111/j.1365-246X.1988.tb00475.x.
Zoeppritz, K., 1919, Erdbebenwellen VIII B, Über Reflexion ad Durchgang seismischer wellen durch Unstetigke itsflachen: Göttinger Nach, 66–84.

Biographies and photographs of the authors are not available.